

Microwave-to-Optical Quantum Transduction via Defect-Mediated Scattering in Diamond

Kyosuke Goto,¹ Hodaka Kurokawa,² Hideo Kosaka,^{1,2,*} and Kazuki Koshino^{3,†}

¹*Department of Physics, Graduate School of Engineering Science, Yokohama National University, 79-5 Tokiwadai, Hodogaya, Yokohama, Kanagawa, 240-8501, Japan*

²*Quantum Information Research Center, Institute of Advanced Sciences,*

Yokohama National University, 79-5 Tokiwadai, Hodogaya, Yokohama, Kanagawa, 240-8501, Japan

³*Institute for Liberal Arts, Institute of Science Tokyo, 2-8-30 Konodai, Ichikawa, Chiba 272-0827, Japan[‡]*

(Dated: May 18, 2026)

Scaling up superconducting quantum processors remains a central challenge for realizing fault-tolerant quantum computation. Although distributed architectures based on optical photons offer a promising route to scalability, they require an efficient microwave-to-optical quantum transducer that operates at cryogenic temperatures. Existing approaches typically rely on strong optical pumping, which induces undesirable heating and degrades single-photon coherence. Here, we propose a microwave-to-optical quantum transducer based on double-resonant scattering from a single color center embedded in a diamond optomechanical resonator. We show that strong coupling between the color center and the optical cavity enables coherent conversion at extremely low pump powers on the order of 10 pW. The proposed device enables remote entanglement generation on the order of 1 kHz with a fidelity exceeding 0.9, demonstrating a viable pathway toward ultra-low-power, high-efficiency quantum transducers based on individual solid-state defects for future distributed superconducting quantum networks.

Fault-tolerant universal quantum computing is expected to require at least several hundred thousand physical qubits [1], posing a major challenge for modern quantum science and technology. To address this scalability issue, distributed quantum computing architectures [2–4] have attracted increasing attention across multiple platforms. For superconducting processors operated at millikelvin temperatures using microwave tones, optical interconnects are attractive because they could enable room-temperature quantum state transfer through flexible, large-bandwidth optical fibers. In practice, however, this approach requires a microwave-to-optical quantum transducer that combines high conversion efficiency with low added noise, which remains an ongoing challenge.

In recent years, substantial progress has been made in microwave-to-optical quantum transducers based on electro-optics [5–7], optomechanics [8–13], magnonics [14], and atomic ensembles [15–20]. A basic strategy is to use small- V , high- Q resonators to enhance the vacuum coupling g between target modes while suppressing unwanted single-photon relaxation. A large g also reduces the required pump power and hence pump-induced heating and added noise. However, overly weak pumping lowers the conversion efficiency. Resolving this efficiency-noise trade-off remains a key challenge for practical microwave-to-optical quantum transducers.

Here we propose an extremely weak-pump quantum transducer based on double-resonant scattering from a single color center in a diamond optomechanical resonator. The scheme exploits the strong coupling of NV^0 to both optical and strain fields by combining the small mode volume of an optomechanical resonator with the resonant dipole transitions of NV^0 . The resulting vacuum coupling strength, more than three orders of

magnitude larger than in conventional optomechanical systems, enables coherent transitions between resonant levels and thus highly efficient conversion under weak pumping. Steady-state analysis shows an external quantum efficiency of 0.32 at a pump power of 55 pW. This enables remote entanglement generation at 3.1 kHz with fidelity 0.93 at a repetition rate of 1 MHz, providing a pathway toward distributed superconducting quantum computers.

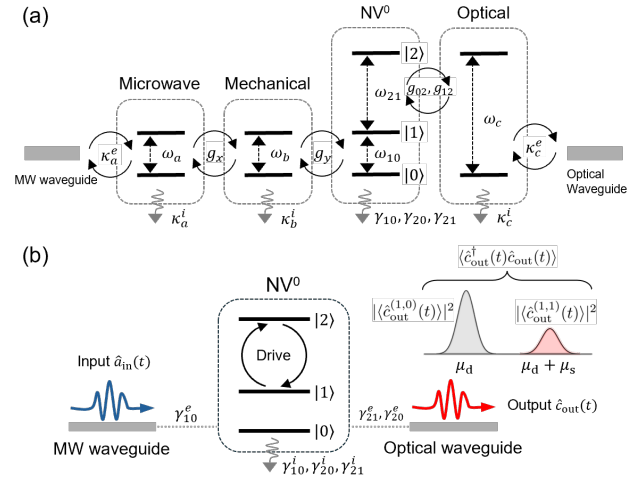


FIG. 1. (a) Mode coupling diagram. We operate in the triply resonant condition where the microwave mode, the mechanical mode, and the $|0\rangle \leftrightarrow |1\rangle$ transition satisfy $\omega_a = \omega_b = \omega_{10}$. The optical mode is tuned to the $|0\rangle \leftrightarrow |2\rangle$ transition. (b) Schematic illustration of the transduction process in the reduced model. The microwave and optical waveguides couple directly to an NV^0 center. A pump tone drives the $|1\rangle \leftrightarrow |2\rangle$ transition resonantly at $\omega_{21} = \omega_{20} - \omega_{10}$.

* kosaka-hideo-yp@ynu.ac.jp

† kazuki.koshino@opticamember.org

‡ Present address: Fujitsu Research Laboratories, Fujitsu Limited

Our quantum transducer consists of a microwave resonator \hat{a} (frequency $\omega_a/2\pi$), a mechanical resonator \hat{b} (frequency

$\omega_b/2\pi$), an NV⁰ center, and an optical resonator \hat{c} (frequency $\omega_c/2\pi$), coupled in series as shown in Fig. 1(a). The NV⁰ center has four ground states formed by orbital states ($|\pm\rangle_o$) and spin states ($|\uparrow\rangle_s, |\downarrow\rangle_s$) [21–23]. We define $\hat{L}_z = \hat{\sigma}_z$ and $\hat{L}_\pm = (\hat{\sigma}_x \pm i\hat{\sigma}_y)/\sqrt{2}$ in the orbital subspace, and $\hat{S}_z = \hat{\sigma}_z/2$ in the spin subspace. The zero-field Hamiltonian is then given by $\hat{H}_{\text{NV}^0}/\hbar = 2\lambda_{\text{so}}\hat{L}_z\hat{S}_z + \epsilon_\perp(\hat{L}_+ + \hat{L}_-)$, where the two terms describe spin-orbit coupling and static strain, respectively. For perturbative strain, the ground states split into two spin-degenerate branches separated by $\Delta_{\text{gs}} = 2\sqrt{\lambda_{\text{so}}^2 + \epsilon_\perp^2} \approx 10$ GHz. Neglecting spin, NV⁰ reduces to a three-level system with lower and upper branches $|0\rangle$ and $|1\rangle$, and orbital excited state $|2\rangle$.

Using this model, the system Hamiltonian is $\hat{H}/\hbar = \omega_a\hat{a}^\dagger\hat{a} + \omega_b\hat{b}^\dagger\hat{b} + \omega_c\hat{c}^\dagger\hat{c} + \omega_{10}\hat{\sigma}_{11} + \omega_{20}\hat{\sigma}_{22} + g_x(\hat{a}^\dagger\hat{b} + \hat{a}\hat{b}^\dagger) + g_y(\hat{b}^\dagger\hat{\sigma}_{01} + \hat{b}\hat{\sigma}_{10}) + g_{02}(\hat{\sigma}_{20}\hat{c} + \hat{\sigma}_{02}\hat{c}^\dagger) + g_{12}(\hat{\sigma}_{21}\hat{c} + \hat{\sigma}_{12}\hat{c}^\dagger)$, where $\hat{\sigma}_{ij} \equiv |i\rangle\langle j|$ ($i, j = 0, 1, 2$) and ω_{ij} is the transition frequency for $|j\rangle \rightarrow |i\rangle$. Here, ω_{10} ($= \Delta_{\text{gs}}$) is a microwave-frequency transition, and ω_{20} is the zero-phonon line (ZPL) of NV⁰. The microwave mode \hat{a} couples to the mechanical mode \hat{b} via the piezoelectric effect with strength g_x , typically $g_x/2\pi \sim 1$ MHz in piezo-optomechanical systems [8–13]. The mechanical mode couples to the $|0\rangle \leftrightarrow |1\rangle$ transition with strength g_y . Although the achievable mechanical coupling for NV⁰ in an optomechanical resonator is not yet known, couplings on the order of 10 MHz have been estimated for other color centers, such as NV⁻ and group-IV color centers including SiV [24, 25], suggesting that $g_y/2\pi \sim 1$ MHz should be feasible. On the optical side, because the cavity linewidth is taken to be broader than ω_{10} , the optical cavity mode \hat{c} , which is resonant with ω_{20} , couples to both the $|0\rangle \leftrightarrow |2\rangle$ and $|1\rangle \leftrightarrow |2\rangle$ transitions. These transitions follow different polarization selection rules and are controllable by the external strain field. In this work, we focus on the strain regime where the $|0\rangle \leftrightarrow |2\rangle$ coupling exceeds the $|1\rangle \leftrightarrow |2\rangle$ coupling (i.e., $g_{02}/2\pi = 1$ GHz and $g_{12}/2\pi = 0.2$ GHz; see Supplemental Material). In the following, we set $\omega_a/2\pi = \omega_b/2\pi = \omega_{10}/2\pi = 10$ GHz, $\omega_{20}/2\pi = \omega_c/2\pi = 500$ THz, and $\omega_{21} = \omega_{20} - \omega_{10}$, unless otherwise specified.

From the full Hamiltonian incorporating all degrees of freedom [Fig. 1(a)], we derive a reduced model [Fig. 1(b)] in which the NV⁰ center couples directly to the waveguides, employing the steady-state approximation to the three cavity modes (see Supplemental Material for derivation). Under the reduced Hamiltonian, the Heisenberg-Langevin equation for $\hat{\sigma}_{ij}$ is $d\hat{\sigma}_{ij}/dt = \sum_{m,n} \left(M_{ij,mn}^{(1)} \hat{\sigma}_{mn} + M_{ij,mn}^{(2)} \hat{a}_{\text{in}}^\dagger(t) \hat{\sigma}_{mn} + M_{ij,mn}^{(3)} \hat{\sigma}_{mn} \hat{a}_{\text{in}}(t) + M_{ij,mn}^{(4)} \hat{c}_{\text{in}}^\dagger(t) \hat{\sigma}_{mn} + M_{ij,mn}^{(5)} \hat{\sigma}_{mn} \hat{c}_{\text{in}}(t) \right)$. Here, $M_{ij,mn}^{(1-5)}$ are coefficient tensors, while $\hat{a}_{\text{in}}(t)$ and $\hat{c}_{\text{in}}(t)$ are the input-field operators from the microwave and optical waveguides, respectively. $M_{ij,mn}^{(1-5)}$ incorporate the relaxation processes through the usual Lindblad-operator formalism. These processes are represented by the effective relaxation rates into the environment, $\gamma_{10}^i = \gamma_{10} + 4g_y^2\kappa_b^i/(\kappa_b^i)^2 + 16g_x^2g_y^2\kappa_a^i/[(\kappa_a^i)^2(\kappa_b^i)^2]$, $\gamma_{20}^i = \gamma_{20} + 4g_{02}^2\kappa_c^i/(\kappa_c^i)^2$, and $\gamma_{21}^i = \gamma_{21} + 4g_{12}^2\kappa_c^i/(\kappa_c^i)^2$, which include both the internal relaxation rates of NV⁰ for each transition

($\gamma_{10}/2\pi = 33$ kHz, $\gamma_{20}/2\pi = 3.5$ MHz, and $\gamma_{21}/2\pi = 3.5$ MHz [21, 23]) and the cavity-mediated contributions, together with the cavity-mediated relaxation into the waveguide modes, $\gamma_{10}^e = 16g_x^2g_y^2\kappa_a^e/[(\kappa_a^e)^2(\kappa_b^e)^2] = 2\pi \times 1.3$ MHz, $\gamma_{20}^e = 4g_{02}^2\kappa_c^e/(\kappa_c^e)^2 = 2\pi \times 14$ MHz, and $\gamma_{21}^e = 4g_{12}^2\kappa_c^e/(\kappa_c^e)^2 = 2\pi \times 0.56$ MHz. Here, κ_A^i , κ_A^e , and κ_A^t denote the internal, external, and total relaxation rates of cavity mode A , respectively (see Supplemental Material for all parameter settings).

In the present device, we simultaneously input a strong classical (coherent-state) drive field from the optical waveguide and a target single photon from the microwave waveguide. However, instead of a single photon, we analyze the case of a coherent-state input also from the microwave waveguide, and *translate* the results to the case of a single-photon input [26, 27]. When the input fields are in the coherent states, the input-field operators are rigorously replaceable with their expectation values as $\hat{a}_{\text{in}}(t) \rightarrow \langle \hat{a}_{\text{in}}(t) \rangle = E_s e^{-i\mu_s t}$ and $\hat{c}_{\text{in}}(t) \rightarrow \langle \hat{c}_{\text{in}}(t) \rangle = E_d e^{-i\mu_d t}$, where E_s (E_d) represents the signal (drive) amplitude and μ_s (μ_d) represents the signal (drive) frequency. In the steady state, the two tones drive oscillations of $\langle \hat{\sigma}_{ij}(t) \rangle$ at harmonic frequencies $p\mu_d + q\mu_s$, where p and q are integers. The signal, drive, and target converted frequencies correspond to $(p, q) = (0, 1)$, $(1, 0)$, and $(1, 1)$, respectively. Using the complex coefficients $s_{ij}^{(p,q)}$, we expand $\langle \hat{\sigma}_{ij}(t) \rangle$ as $\langle \hat{\sigma}_{ij}(t) \rangle = \sum_{p,q} s_{ij}^{(p,q)} e^{-it(p\mu_d + q\mu_s)}$. Substituting this expression into $d\langle \hat{\sigma}_{ij} \rangle/dt$ yields simultaneous equations for $s_{ij}^{(p,q)}$.

Using $\langle \hat{\sigma}_{ij} \rangle$ obtained by solving these simultaneous equations, and the optical input-output relation $\hat{c}_{\text{out}}(t) = \hat{c}_{\text{in}}(t) - i\sqrt{\gamma_{21}^e} \hat{\sigma}_{12} - i\sqrt{\gamma_{20}^e} \hat{\sigma}_{02}$, we calculate the output-field amplitude $\langle \hat{c}_{\text{out}}(t) \rangle$ and photon flux $\langle \hat{c}_{\text{out}}^\dagger(t) \hat{c}_{\text{out}}(t) \rangle$ of the light output through the optical waveguide. Here, rapidly oscillating components of $\langle \hat{c}_{\text{out}}^\dagger(t) \hat{c}_{\text{out}}(t) \rangle$ are negligible because they are not detected. We assume that the drive frequency (μ_d) component of the output field is separable from the converted frequency ($\mu_d + \mu_s$) component by a frequency filter, thanks to the large frequency difference. Then, the total detected photon flux is $R_{\text{tot}} = \langle \hat{c}_{\text{out}}^\dagger(t) \hat{c}_{\text{out}}(t) \rangle - |\langle \hat{c}_{\text{out}}^{(1,0)}(t) \rangle|^2$, where $\langle \hat{c}_{\text{out}}^{(p,q)}(t) \rangle \propto e^{-it(p\mu_d + q\mu_s)}$ denotes the field-amplitude component oscillating at $p\mu_d + q\mu_s$. We neglect $|\langle \hat{c}_{\text{out}}^{(1,-1)}(t) \rangle|^2$ and the higher-order sidebands, which are numerically confirmed to be negligibly small. Note that R_{tot} contains incoherent emission arising from the color-center nonlinearity. The coherent photon flux at $\mu_d + \mu_s$ is given by $R_{\text{coh}} = |\langle \hat{c}_{\text{out}}^{(1,1)}(t) \rangle|^2$, which retains the indistinguishability of the input microwave photon.

To calculate the single-photon response, we use the correspondence between coherent and number states. Expanding a coherent state $|\alpha\rangle$ in the photon-number basis shows that the amplitude of the $|1\rangle$ component is proportional to $e^{-|\alpha|^2/2}\alpha$. Thus, in the limit $|\alpha|^2 \ll 1$, the term proportional to $|\alpha|^2$ in the expectation value for a coherent-state input corresponds to that for a single-photon input. Accordingly, we expand R_{tot} and R_{coh} as Taylor series in the signal photon flux $|E_s|^2$ and identify the coefficients of the linear terms as the single-photon response.

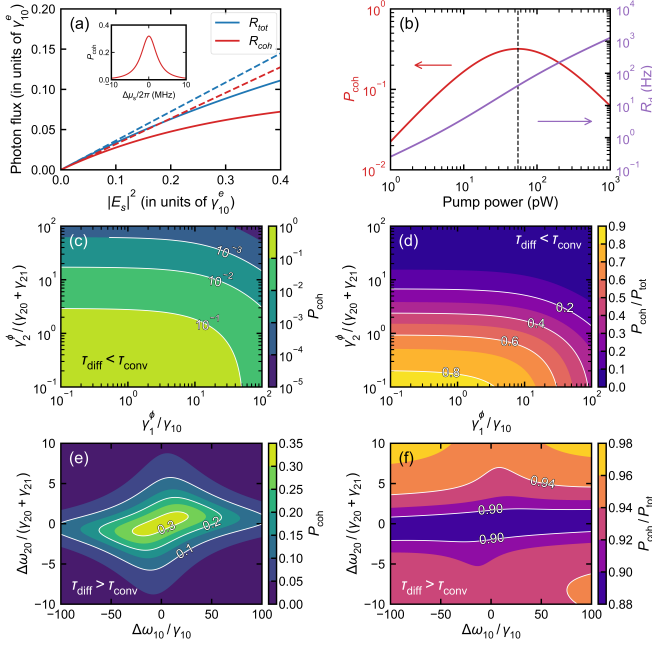


FIG. 2. Single-photon conversion process. (a) Total detected photon flux R_{tot} (blue) and coherent photon flux R_{coh} (red) as functions of incident signal microwave photon flux $|E_s|^2$. The dashed lines indicate the tangents at the origin; their slopes give the corresponding conversion efficiencies for a single incident microwave photon, P_{tot} and P_{coh} , obtained by linear regression. The inset shows P_{coh} as a function of the signal-frequency detuning $\Delta\mu_s$. The conversion bandwidth is determined from the full width at half maximum of the curve shown in the inset. (b) Coherent conversion efficiency P_{coh} (red) and dark count rate (purple) versus pump power. The vertical dotted line indicates 55 pW. (c) P_{coh} and (d) $P_{\text{coh}}/P_{\text{tot}}$ as functions of the pure dephasing rates $\gamma_1^\phi, \gamma_2^\phi$ for $\tau_{\text{diff}} < \tau_{\text{conv}}$. (e) P_{coh} and (f) $P_{\text{coh}}/P_{\text{tot}}$ as functions of detunings from resonance, $\Delta\omega_{10}$ and $\Delta\omega_{20}$ for $\tau_{\text{diff}} > \tau_{\text{conv}}$. In these panels, the signal and drive frequencies are on resonance with ω_{10} and ω_{20} , respectively (i.e., $\mu_s = \omega_{10}$ and $\mu_d = \omega_{21}$).

The total detection probability P_{tot} and coherent conversion efficiency P_{coh} are therefore given by $P_{\text{tot}} = \lim_{|E_s|^2 \rightarrow 0} \frac{dR_{\text{tot}}}{d|E_s|^2}$ and $P_{\text{coh}} = \lim_{|E_s|^2 \rightarrow 0} \frac{dR_{\text{coh}}}{d|E_s|^2}$. For a pump power of $\hbar\mu_d|E_d|^2 = 55$ pW, we obtain $P_{\text{tot}} = 0.36$ and $P_{\text{coh}} = 0.32$, respectively, from the slopes of R_{tot} and R_{coh} at the origin [Fig. 2(a)]. Their difference $P_{\text{tot}} - P_{\text{coh}}$ represents the detection probability P_{inc} of incoherent photons generated by spontaneous emission after dephasing at the NV^0 excited state $|2\rangle$. As discussed in the Supplemental Material, it is noteworthy that these results agree well with the pump power and P_{coh} estimated using a phenomenological model that is analytically tractable. We also determine the conversion bandwidth by calculating P_{coh} as a function of the signal-frequency detuning $\Delta\mu_s = \mu_s - \omega_{10}$, obtaining $BW = 5.0$ MHz. This value is approximately consistent with $(\gamma_{20} + \gamma_{21})/2\pi$. Thus, the emission from NV^0 has relaxed by 98% after $\tau_{\text{conv}} \sim 4/(2\pi \cdot BW) = 130$ ns. Even in the absence of a signal, the drive weakly excites NV^0 and yields a dark count rate $R_d = \lim_{|E_s|^2 \rightarrow 0} R_{\text{tot}} = 41$ Hz. As shown in Fig. 2(b), in this weak-pump regime, R_d increases linearly with

the pump power.

Spectral diffusion is also a significant issue for color centers. In this paper, we distinguish two regimes according to the relative magnitudes of the spectral-diffusion timescale τ_{diff} and the conversion timescale τ_{conv} , and analyze each case separately. When $\tau_{\text{diff}} < \tau_{\text{conv}}$, spectral diffusion can be modeled by introducing pure dephasing rates γ_1^ϕ and γ_2^ϕ for the levels $|1\rangle$ and $|2\rangle$, respectively, into $M_{ij,mn}^{(1)}$ in the Heisenberg-Langevin equation. Treating γ_1^ϕ and γ_2^ϕ as parameters, we calculate the steady-state response and find that both P_{coh} and the coherent-photon fraction $P_{\text{coh}}/P_{\text{tot}}$ decrease as the pure dephasing rates increase [Figs. 2(c) and 2(d)]. This reflects the loss of coherence caused by the decay of the off-diagonal density-matrix elements due to spectral diffusion. These figures also show that, near $\gamma_1^\phi/2\pi \sim 50\gamma_{10}/2\pi = 1.7$ MHz and $\gamma_2^\phi/2\pi \sim 1.5(\gamma_{20} + \gamma_{21})/2\pi = 11$ MHz, respectively, $P_{\text{coh}} \sim 0.1$ and $P_{\text{coh}}/P_{\text{tot}} \sim 0.5$. These rates are close to the cavity-mediated waveguide coupling rates, $\gamma_{10}^e/2\pi = 1.3$ MHz and $\gamma_{20}^e/2\pi = 14$ MHz, suggesting that the incoherent component becomes dominant once the coherence decays exceed the cavity-mediated external coupling rates to the waveguides.

By contrast, when $\tau_{\text{diff}} > \tau_{\text{conv}}$, fluctuations in the energy levels are negligible during the conversion process. It is of note that artificial extension of τ_{diff} is possible using resonance-check (RC) techniques [28, 29]. In this case, spectral diffusion can be modeled as constant detunings, $\omega_{10}/2\pi = 10$ GHz + $\Delta\omega_{10}/2\pi$ and $\omega_{20}/2\pi = 500$ THz + $\Delta\omega_{20}/2\pi$. We then evaluate P_{coh} and $P_{\text{coh}}/P_{\text{tot}}$ by substituting these expressions for ω_{10} and ω_{20} into $M_{ij,mn}^{(1)}$ and sweeping $\Delta\omega_{10}$ and $\Delta\omega_{20}$ [Figs. 2(e) and 2(f)]. Fig. 2(e) shows that, in order to achieve conversion with $P_{\text{coh}} \geq 0.1$, the magnitude of transition-frequency fluctuation must satisfy $|\Delta\omega_{10}| \lesssim 50\gamma_{10}$ and $|\Delta\omega_{20}| \lesssim 1.5(\gamma_{20} + \gamma_{21})$. If the long-time-averaged photoluminescence excitation (PLE) spectrum is well described by a Gaussian profile, the PLE linewidth Γ and the standard deviation σ of $\Delta\omega_{20}$ are related by $\Gamma \approx 2.36\sigma$. Since approximately 95% of a Gaussian distribution lies within $\pm 1.96\sigma$, the condition $|\Delta\omega_{20}| \lesssim 1.5(\gamma_{20} + \gamma_{21})$ is met with about 95% probability for $\Gamma \lesssim 1.81(\gamma_{20} + \gamma_{21}) = 2\pi \times 50$ MHz. Under this condition, $P_{\text{coh}} \geq 0.1$ can be achieved with high probability. The incoherent contribution from spontaneous emission is therefore reduced, so $P_{\text{coh}}/P_{\text{tot}}$ increases, as seen in Fig. 2(f). Thus, although detuning lowers the efficiency, operation with $P_{\text{coh}}/P_{\text{tot}} \geq 0.9$ is possible for detunings of about 10 MHz.

So far, we have discussed the conversion characteristics of the transducer. We now turn to remote entanglement generation using the converted *communication* photons. To realize distributed quantum computing across different dilution refrigerators, quantum entanglement shared between superconducting qubits serves as a fundamental resource for implementing non-local quantum operations [30]. For superconducting qubits, remote entanglement is generated by frequency-converting photons entangled with superconducting qubits, then interfering photons using a beam splitter and single-photon detectors [Fig. 3(a)]. Here, we consider the single-click scheme [31]. In this scheme, the fidelity of the generated entangled state is degraded not only by reduced indistinguishability due to loss of

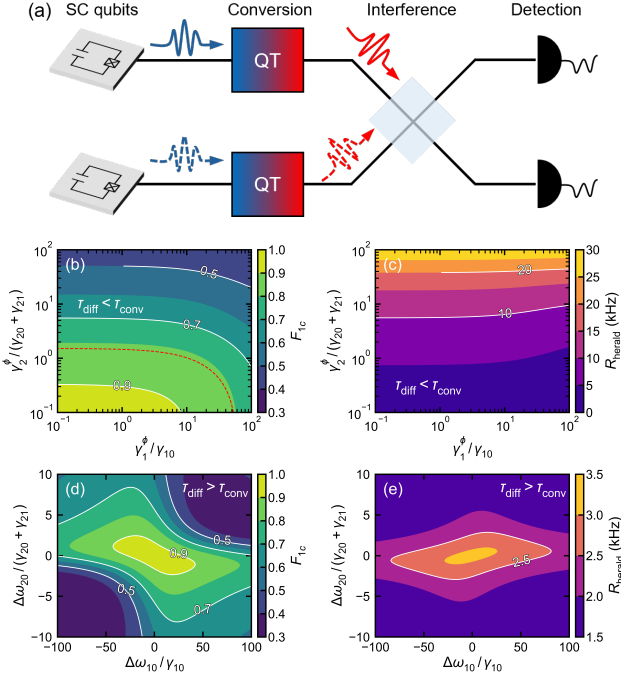


FIG. 3. Remote entanglement generation. (a) Microwave photons entangled with superconducting qubits (SC qubits) are converted into optical photons by quantum transducers (QTs) and injected into an interferometer, generating remote entanglement. (b) Fidelity and (c) heralding rate as functions of the pure-dephasing rates γ_1^ϕ and γ_2^ϕ for $\tau_{\text{diff}} < \tau_{\text{conv}}$. The red dashed line indicates the contour $P_{\text{coh}}^{(A)}/P_{\text{tot}}^{(A)} = 0.5$. (d) Fidelity and (e) heralding rate as functions of the detunings $\Delta\omega_{10}$ and $\Delta\omega_{20}$ for $\tau_{\text{diff}} > \tau_{\text{conv}}$.

the photon coherence and by false detections caused by noise, but also by phase differences between the interference paths, which modify the relative phase of the generated entangled state. To generate a high-fidelity entangled state, the qubit excitation probability P_e must be made sufficiently larger than the noise-detection probability P_d , while double-excitation events in which both nodes are excited must be suppressed ($P_d \ll P_e \ll 1$).

The effect of the transducer at node i ($= A, B$) on the interference path is modeled by a composite channel $\tilde{\mathcal{E}}_i = \mathcal{N}_i \circ \mathcal{E}_i$, where \mathcal{E}_i is a quantum channel that converts the input photon with probability $P_{\text{tot}}^{(i)}$ and imparts a phase θ_i to the converted photon, whereas \mathcal{N}_i adds a noise photon with probability $P_d^{(i)}$. Here, θ_i is defined as the phase-space argument of the single-photon component of $\langle \hat{c}_{\text{out}}^{(1,1)}(t) \rangle$. With both the drive-pulse length and the photon-detection time window set to τ_{conv} , the noise-addition probability is given by $P_d^{(i)} = \tau_{\text{conv}} R_d^{(i)}$. Because the converted photon is transformed into an incoherent photon with probability $P_{\text{inc}}^{(i)}/P_{\text{tot}}^{(i)}$, the channel \mathcal{E}_i also incorporates this process. Since we consider entanglement generation over short distances of about 10 m, we neglect losses other than those due to the transducers and assume that the interference paths themselves are phase locked. Restricting attention to the regime in which two-photon detection

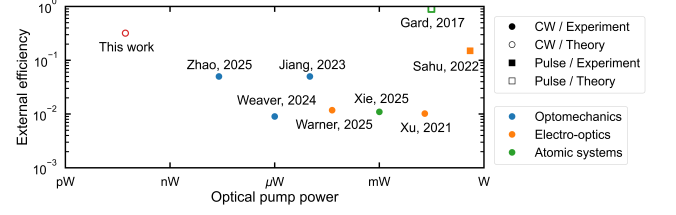


FIG. 4. Comparison of conversion efficiency versus pump power with the literature. References: Zhao, 2025 [13]; Weaver, 2024 [11]; Jiang, 2023 [9]; Warner, 2025 [7]; Xie, 2025 [20]; Xu, 2021 [5]; Gard, 2017 [32]; Sahu, 2022 [6].

events at the same detector are negligible, the fidelity with respect to the target Bell state $|\Psi^+\rangle = (|10\rangle + |01\rangle)/\sqrt{2}$ is given by $F_{1c} = \frac{1}{\mathcal{N}} \left[\Pi_{10} + \Pi_{01} + \alpha|\delta| \cos \theta \right] P_e (1 - P_e)$ with $\mathcal{N} = 2 \left[(1 - P_e)^2 \Pi_{00} + P_e (1 - P_e) (\Pi_{10} + \Pi_{01}) + P_e^2 \Pi_{11} \right]$. Here, \mathcal{N} is the total single-click probability, while Π_{ij} , ($i, j = 0, 1$) are the effective single-click weights associated with the input photon-number state $|ij\rangle$. The term $\alpha|\delta| \cos \theta$ denotes the interference contribution, where $\alpha = (1 - P_d^{(A)}/2)(1 - P_d^{(B)}/2)$, $\delta = \sqrt{P_{\text{coh}}^{(A)} P_{\text{coh}}^{(B)}} e^{-i\theta}$, and $\theta = \theta_A - \theta_B$ is the phase difference between the two paths; see Supplemental Material for details. In the following calculations, we set $P_e = \sqrt{\Pi_{00}} / (\sqrt{\Pi_{00}} + \sqrt{\Pi_{11}})$, at which F_{1c} is maximized. If entanglement generation is attempted at a repetition rate R_{rep} , the heralding rate is approximately given by $R_{\text{herald}} \sim \mathcal{N} R_{\text{rep}}$.

Using F_{1c} and R_{herald} , we calculate the fidelity of the entangled state and the heralding rate at a repetition rate of $R_{\text{rep}} = 1$ MHz for the general case including spectral diffusion. For simplicity, we consider only the case in which spectral diffusion is present in the transducer at node A, while the transducer at node B is treated as ideal. First, for $\tau_{\text{diff}} < \tau_{\text{conv}}$, phase fluctuations are effectively averaged out and have little impact; the fidelity is therefore governed primarily by the coherence of the emitted photons. As shown in Fig. 3(b), $F_{1c} \sim 0.8$ at $P_{\text{coh}}^{(A)}/P_{\text{tot}}^{(A)} = 0.5$. This suggests that F_{1c} approximately scales as $(1 + P_{\text{coh}}^{(A)}/P_{\text{tot}}^{(A)})/2$. By contrast, when $P_{\text{coh}}^{(A)}/P_{\text{tot}}^{(A)} \lesssim 0.1$, i.e., $\gamma_2^\phi \gtrsim 15(\gamma_{20} + \gamma_{21})$, interference is almost completely suppressed and $F_{1c} \lesssim 0.5$. In this regime, the increase in P_d also enhances R_{herald} , as shown in Fig. 3(c), revealing a trade-off between fidelity and heralding rate. In contrast, for $\tau_{\text{diff}} > \tau_{\text{conv}}$, detuning from resonance causes a substantial phase rotation and hence a pronounced reduction in F_{1c} . In Fig. 3(d), the region with $F_{1c} \gtrsim 0.8$ corresponds to the regime where $\cos \theta \gtrsim 0.8$, whereas the contour $F_{1c} = 0.5$ approximately marks a phase rotation of $\pi/2$. For the ideal detuning condition $(\Delta\omega_{10}, \Delta\omega_{20}) = (0, 0)$, the fidelity reaches $F_{1c} = 0.93$. The corresponding heralding rate is $R_{\text{herald}} = 3.1$ kHz, as shown in Fig. 3(e).

Finally, we compare the external efficiency versus pump power for this work and previous studies [Fig. 4]. Owing to the large dipole-cavity coupling achieved by coupling a single color center to small-mode-volume resonators, the optimal pump

power for $\sim 10\%$ efficiency is more than three orders of magnitude lower than those in current electro-optic, optomechanical, and atomic-ensemble systems. Such a reduction would suppress both pump-induced heating and noise, and increase the number of transducers that can be integrated into a dilution refrigerator, thereby enabling power-efficient large-scale integration.

In this work, we have proposed an extremely low-pump microwave-to-optical quantum transducer based on a diamond optomechanical resonator containing a single NV⁰ center. Our model yields a coherent conversion efficiency of 0.32 at a pump power of 55 pW, enabling remote entanglement generation at a rate of ~ 1 kHz with fidelity above 0.9. While color centers offer these advantages, we also identify a challenge: spectral diffusion, for example from charge noise. When it occurs faster than the cavity-mediated waveguide coupling, incoherent emission dominates and significantly degrades the fidelity of remote entanglement generation based on photon interference.

Thus, future research directions include mitigating such charge noise by improving fabrication conditions and exploring color centers that are robust against charge noise, as exemplified by SiV centers in diamond, while also seeking systems with small spin-orbit coupling (< 10 GHz). Despite this challenge, the proposed transducer is a promising microwave-to-optical interface and a foundation for future large-scale distributed quantum computing.

H. Kosaka acknowledges the funding support from Japan Science and Technology Agency (JST) Moonshot R&D grant (JPMJMS2062) and JST CREST grant (JPMJCR1773). H. Kosaka also acknowledges the Ministry of Internal Affairs and Communications (MIC) for funding, R&D for construction of global quantum cryptography network (JPMI00316), R&D of ICT Priority Technology Project, and the Japan Society for the Promotion of Science (JSPS) Grants-in-Aid for Scientific Research (20H05661, 20K20441, 25H0083050).

-
- [1] C. Gidney and M. Ekerå, *Quantum* **5**, 433 (2021).
- [2] N. H. Nickerson, Y. Li, and S. C. Benjamin, *Nature Communications* **4**, 1756 (2013).
- [3] D. Main, P. Drmota, D. P. Nadlinger, E. M. Ainley, A. Agrawal, B. C. Nichol, R. Srinivas, G. Araneda, and D. M. Lucas, *Nature* **638**, 383 (2025).
- [4] M. J. Weaver, G. Arnold, H. Weaver, S. Gröblacher, and R. Stockill, *Scalable quantum computing with optical links* (2025), [arXiv:2505.00542 \[quant-ph\]](https://arxiv.org/abs/2505.00542).
- [5] Y. Xu, A. Al Sayem, L. Fan, C. Zou, S. Wang, R. Cheng, W. Fu, L. Yang, M. Xu, and H. X. Tang, *Nature Communications* **12**, 4453 (2021).
- [6] R. Sahu, W. Hease, A. Rueda, G. Arnold, L. Qiu, and J. M. Fink, *Nature Communications* **13**, 1276 (2022).
- [7] H. K. Warner, J. Holzgrafe, B. Yankelevich, D. Barton, C. J. Xin, N. Sinclair, D. Zhu, A. Shams-Ansari, G. Joe, M. Loncar, S. Polletto, E. Sete, B. Langley, M. J. Reagor, E. Batson, M. Colangelo, K. K. Berggren, and L. Jiang, *Nature Physics* **21**, 831 (2025).
- [8] M. Mirhosseini, A. Sipahigil, M. Kalaei, and O. Painter, *Nature* **588**, 599 (2020), published: 23 December 2020. Contributed equally (as indicated on the journal page).
- [9] W. Jiang, F. M. Mayor, S. Malik, R. Van Laer, T. P. McKenna, R. N. Patel, J. D. Witmer, and A. H. Safavi-Naeini, *Nature Physics* **19**, 1423 (2023).
- [10] S. Meesala, S. Wood, D. Lake, P. Chiappina, C. Zhong, A. D. Beyer, M. D. Shaw, L. Jiang, and O. Painter, *Nature Physics* **20**, 871 (2024).
- [11] M. J. Weaver, P. Duivesteyn, A. C. Bernasconi, S. Scharmer, M. Lemang, T. C. van Thiel, F. Hijazi, B. Hensen, S. Gröblacher, and R. Stockill, *Nature Nanotechnology* **19**, 166 (2024), published online 05 Oct 2023.
- [12] T. C. van Thiel, M. J. Weaver, F. Berto, P. Duivesteyn, M. Lemang, K. L. Schuurman, M. Žemlička, F. Hijazi, A. C. Bernasconi, C. Ferrer, E. Cataldo, E. Lachman, M. Field, Y. Mohan, F. K. de Vries, C. C. Bultink, J. C. van Oven, J. Y. Mutus, R. Stockill, and S. Gröblacher, *Nature Physics* **21**, 401 (2025).
- [13] H. Zhao, W. D. Chen, A. Kejriwal, and M. Mirhosseini, *Nature Nanotechnology* **20**, 602 (2025), epub 2025-03-13. Contributed equally (as indicated on the journal/PubMed record).
- [14] R. Hisatomi, A. Osada, Y. Tabuchi, T. Ishikawa, A. Noguchi, R. Yamazaki, K. Usami, and Y. Nakamura, *Phys. Rev. B* **93**, 174427 (2016).
- [15] J. Han, T. Vogt, C. Gross, D. Jaksch, M. Kiffner, and W. Li, *Phys. Rev. Lett.* **120**, 093201 (2018).
- [16] T. Vogt, C. Gross, J. Han, S. B. Pal, M. Lam, M. Kiffner, and W. Li, *Phys. Rev. A* **99**, 023832 (2019).
- [17] H.-T. Tu, K.-Y. Liao, Z.-X. Zhang, X.-H. Liu, S.-Y. Zheng, S.-Z. Yang, X.-D. Zhang, H. Yan, and S.-L. Zhu, *Nature Photonics* **16**, 291 (2022), published online 28 Feb 2022.
- [18] J. Rochman, T. Xie, J. G. Bartholomew, K. C. Schwab, and A. Faraon, *Nature Communications* **14**, 1153 (2023), published 2023-03-01.
- [19] S. Borówka, U. Pylypenko, M. Mazelanik, and M. Parniak, *Nature Photonics* **18**, 32 (2024), published online 05 Oct 2023.
- [20] T. Xie, R. Fukumori, J. Li, and A. Faraon, *Nature Physics* **21**, 931 (2025).
- [21] J. Baier, C. E. Bradley, T. Middelburg, V. V. Dobrovitski, T. H. Taminiou, and R. Hanson, *Physical Review Letters* **125**, 193601 (2020).
- [22] H. Kurokawa, K. Wakamatsu, S. Nakazato, T. Makino, H. Kato, Y. Sekiguchi, and H. Kosaka, *Nature Communications* **15**, 4039 (2024).
- [23] H. Kurokawa, S. Nakazato, T. Makino, H. Kato, S. Onoda, Y. Sekiguchi, and H. Kosaka, *Physical Review Letters* **135**, 016902 (2025).
- [24] B. Kim, H. Kurokawa, K. Sakai, K. Koshino, H. Kosaka, and M. Nomura, *Physical Review Applied* **20**, 044037 (2023).
- [25] G. Joe, M. Haas, K. Kuruma, C. Jin, D. D. Kang, S. W. Ding, C. Chia, H. Warner, B. Pingault, B. Machielse, S. Meesala, and M. Loncar, Observation of the acoustic purcell effect with a color-center and a nanomechanical resonator (2025), [arXiv:2503.09946v2](https://arxiv.org/abs/2503.09946v2), [arXiv:2503.09946 \[quant-ph\]](https://arxiv.org/abs/2503.09946).
- [26] K. Koshino and H. Ishihara, *Phys. Rev. Lett.* **93**, 173601 (2004).
- [27] K. Koshino, *Phys. Rev. Lett.* **98**, 223902 (2007).
- [28] J. M. Brevoord, L. De Santis, T. Yamamoto, M. Pasini, N. Co-dreanu, T. Turan, H. K. Beukers, C. Waas, and R. Hanson, *Phys. Rev. Appl.* **21**, 054047 (2024).
- [29] S. L. N. Hermans, M. Pompili, L. Dos Santos Martins, A. R. P. Montblanch, H. K. C. Beukers, S. Baier, J. Borregaard, and R. Hanson, *New Journal of Physics* **25**, 013011 (2023).
- [30] P. Kurpiers, P. Magnard, T. Walter, B. Royer, M. Pechal, J. Heinsoo, Y. Salathé, A. Akin, S. Storz, J.-C. Besse, S. Gasparinetti,

- A. Blais, and A. Wallraff, [Nature](#) **558**, 264 (2018).
- [31] C. Cabillo, J. I. Cirac, P. García-Fernández, and P. Zoller, [Phys. Rev. A](#) **59**, 1025 (1999).
- [32] B. T. Gard, K. Jacobs, R. McDermott, and M. Saffman, [Phys. Rev. A](#) **96**, 013833 (2017).